Non-unit protection method for long transmission lines in MTDC grids

Mirhosseini, Seyed Sattar; Jamali, Sadegh; Popov, Marjan

DOI
10.1049/gtd2.12125

Publication date
2021

Document Version
Final published version

Published in
IET Generation, Transmission and Distribution

Citation (APA)
Mirhosseini, S. S., Jamali, S., & Popov, M. (2021). Non-unit protection method for long transmission lines in MTDC grids. *IET Generation, Transmission and Distribution*, *15*(11), 1674-1687. https://doi.org/10.1049/gtd2.12125

Received: 18 May 2020 | Revised: 19 November 2020 | Accepted: 4 January 2021

DOI: 10.1049/gtd2.12125

IET Generation, Transmission & Distribution

The Institution of Engineering and Technology WILEY

ORIGINAL RESEARCH PAPER

Non-unit protection method for long transmission lines in MTDC grids

Seyed Sattar Mirhosseini[1,2] | **Sadegh Jamali**[1] | **Marjan Popov**[2]

[1] Centre of Excellence for Power System Automation and Operation, School of Electrical Engineering, Iran University of Science and Technology, Tehran, Iran

[2] Faculty of Electrical Engineering, Mathematics and Computer Science, Delft University of Technology, Delft 2628 CD, The Netherlands

Correspondence
Sadegh Jamali, Centre of Excellence for Power System Automation and Operation, School of Electrical Engineering, Iran University of Science and Technology,16846-13114, Tehran, Iran.
Email: sjamali@iust.ac.ir

Abstract

This paper presents a non-unit protection method for long transmission lines of multi-terminal HVDC (MTDC) grids based on the magnitude and direction of modal voltage and current travelling waves. The method overcomes the difficulty resulting from high attenuation and distortion as reported in previous methods using fault-generated transients for protection of long HVDC lines. The proposed method determines the faulted pole using multi-resolution morphological gradient of the pole voltage. Then, the multiplication of multi-resolution morphological gradient of the modal travelling waves is utilised as a criterion to discriminate between internal and external faults and non-fault events. The criterion is a negative high value for internal faults, a negative low value for forward external faults and events, and a positive value for backward external faults and events. A four-terminal HVDC grid with modular multilevel converters including long HVDC lines is modelled using the PSCAD/EMTDC software. The simulation study validates effectiveness of the method for detection and discrimination of high resistance faults on long lines, as well as stability against external DC and AC faults, and DC circuit breaker opening and reclosing transients. The proposed method uses a relatively low sampling frequency and local data, i.e. no requirement for a communication link.

1 | INTRODUCTION

Multi-terminal HVDC (MTDC) grids with voltage source converter (VSC) are identified as a key solution for the integration of renewable energy resources, particularly offshore wind farms, into existing power systems [1–3]. MTDC grids should have reliable protection to rapidly locate and isolate a faulted line or device in order to ensure that the remaining parts of the grid resume power supply service. DC fault currents are characterised by high rates of rise and amplitudes, which make converter power electronic devices very vulnerable, and imposes high demands on the DC circuit breaker (DCCB) for prompt current interruption. In order to meet these requirements, the protection should be reliable and capable of operating in a few milliseconds [3–6].

A method using voltage and current magnitudes and their directions to detect and identify the faulted line is presented in [7]. It starts by blocking the converters, operation of AC and some DCCBs and fast DC switches. Then, the rest of the grid is restarted by de-blocking the converters. The weakness of this method is the complete grid shut down, which results in power supply disruption. A protection method based on voltage and current magnitude and their derivatives is proposed and tested for a radial MTDC grid in [8]. This method is applicable for 2-level VSCs in which the DC capacitors located at each terminal divide the grid into different protection zones by supplying large fault currents. However, for modular multilevel converter (MMC) based grids, DC capacitors are distributed inside the sub-modules and their discharge is limited by the arm reactors. A protection method utilizing the maximum of the DC voltage derivative is proposed in [9]. In [10], the same author deploys the ratio of the peak voltage derivative at both sides of the series inductor to determine a fault direction and to improve the previous method. These methods are tested for a radial bipolar HVDC grid. A protection method combining overcurrent, undervoltage, and current derivative is proposed and tested for relatively low resistance faults in [11]. A protection scheme using wavelet coefficients of voltages and currents, and voltage

---

magnitude and derivative is proposed in [3]. The voltage magnitude and derivative are applied to cover insufficiency of the wavelet coefficients in the discrimination of the faulted cable. This scheme is tested on a 2-level VSC, but it is only evaluated for bolted faults. The methods based on the calculation of voltage and current derivatives can be easily affected by measurement noise. Moreover, the generated transients during DCCB opening at the adjacent lines may affect the correct operation of the protection system.

The protection methods using the rate of voltage change across the series inductor with predefined voltage thresholds are proposed in [12, 13]. This is equivalent to the second derivative of the DC current, which leads to better electromagnetic interference prevention. A protection method based on the ratio of mid-band frequency transient voltage measured at the line side of the series inductor to mid-band frequency transient voltage measured at the DC terminal capacitor is presented in [14]. The methods in [12–14] require an additional voltage divider to measure the voltage across the series inductor and DC terminal capacitor. A protection scheme using the first peak time of the filtered DC voltage is proposed and tested for relatively short overhead lines in [15].

Current differential protection using communication links between line ends is presented in [16–18], and protection methods using the polarity of the fault current component at both ends of the cable are proposed in [19, 20]. Two wide area faulted line identification and fault point location methods based on travelling wave arrival times are proposed in [21, 22]. These methods need global positioning system signal and communication links all over the grid. The main drawbacks of the differential protection and other communication-based protections are additional costs and reduced reliability due to the risk of communication media failure. Moreover, they introduce an undesirable communication delay, especially in the protection of long transmission lines.

A protection method using wavelet decomposition energy and principal component analysis of local DC current as an input for a genetic fuzzy system is presented in [23]. It is evaluated for a radial MTDC and it is only applicable to relatively low resistance faults. The applicability of such methods to other grids is conditioned by having a new training data set. By using several optical sensors distributed along the cable, in [24] a protection method is presented to identify the faulted line by calculating the differential current of two consecutive sensors. The same technique is used in [25] to protect cables using directional sequence protection and the reclosing capability of proactive hybrid DCCBs. The use of distributed sensors along the cable improves the performance of the protection system, especially when using long cables; however, it results in higher costs, and risk of sensor failure. A protection method based on wavelet transform of modal voltage travelling waves is proposed and tested for relatively short overhead lines in [26]. A protection method based on high frequency modal transient voltage energy by applying wavelet transform is presented and tested for relatively short cables and overhead lines in [27]. In [28] an improved travelling wave method is presented with adaptive thresholds determined by the estimation of fault impedance using a curve fitting method. The method is tested for high resistance faults occurring on relatively long overhead lines. Another improved travelling wave protection method using high frequency components of line voltages and currents obtained by wavelet transform is presented in [29]. The method is verified for a radial MTDC grid for high resistance faults occurring on a long overhead line. A protection method using mathematical morphology gradient to detect fault-generated voltage travelling wave fronts is proposed by [30]. This method is tested for both cable and overhead transmission lines; however, it is not suitable for long cables. A protection method that uses the median absolute deviation of the voltage and current is presented in [31], and it is tested by a real-time digital simulator for relatively long cables. Although this method is very robust, it still needs improvements for high resistance faults.

The protection of long lines, especially cables, in MTDC grids is a challenging issue due to the high attenuation and distortion of travelling waves. Non-unit protection, as a main option for primary protection, has inherent limitations regarding the line length. Communication-based methods are not limited in theory but, as mentioned, their intrinsic delay and risk of communication failure make them unsuitable as primary protection. Moreover, in practice, the complexity of such methods increases for long cables [25]. The protection methods utilizing distributed sensors along the cable are complex, costly and risky because of sensor failure. Therefore, it is imperative to develop non-unit methods, which are capable of protecting long lines.

In this paper, the magnitude and the relative direction of the line mode voltage and current travelling wave fronts determined by multi-resolution morphological gradients are deployed to overcome the problem of non-unit protection of long transmission lines in MTDC grids. The method is verified using MATLAB by calculating multi-resolution morphological gradient, and PSCAD to model a four-terminal MMC based HVDC grid.

The rest of the paper is organized as follows: Section 2 presents the basic theory of travelling wave and multi-resolution morphology. The proposed protection method is introduced in Section 3. Section 4 demonstrates the protection criteria. The protection method is assessed in Section 5. The proposed protection method is compared to other works in Section 6 and meaningful conclusions are provided in Section 7.

2 | BASIC THEORY

2.1 | Travelling wave theory

Figure 1 shows a distributed parameter model of an HVDC line in which Z_s and Y_s are the series impedance and shunt admittance of the positive and negative pole lines, and Z_m and Y_m denote the mutual impedance and admittance between the lines. V_p, I_p and V_n, I_n denote the voltage and current at the positive and negative poles, respectively. In order to remove the electromagnetic coupling between the positive and negative lines, especially in case of overhead line, the pole quantities can be

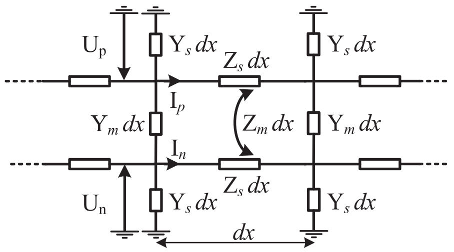

FIGURE 1 The distributed model of bipolar HVDC line

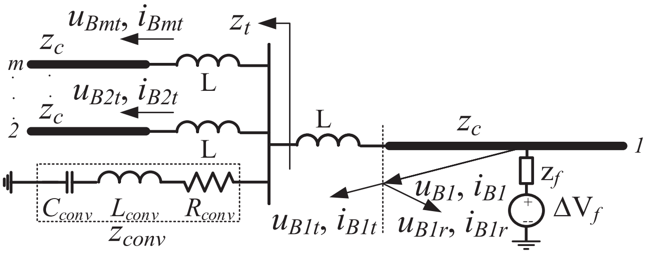

FIGURE 2 A DC terminal in MTDC grid

transformed to ground and line mode quantities using the modal transformation matrix [32], as follows:

$$\begin{bmatrix} V_l \\ V_g \end{bmatrix} = \frac{1}{\sqrt{2}} \begin{bmatrix} 1 & -1 \\ 1 & 1 \end{bmatrix} \begin{bmatrix} V_p \\ V_n \end{bmatrix} \tag{1}$$

$$\begin{bmatrix} I_l \\ I_g \end{bmatrix} = \frac{1}{\sqrt{2}} \begin{bmatrix} 1 & -1 \\ 1 & 1 \end{bmatrix} \begin{bmatrix} I_p \\ I_n \end{bmatrix} \tag{2}$$

where V_l and I_l are the line mode voltage and current, and V_g and I_g are the ground mode voltage and current.

According to the theory of travelling waves, a fault or any sudden change in the line voltage generates voltage and current travelling waves moving away from the fault point in both directions. The voltage and the current at each point x of the line is given as sum of forward and backward travelling waves. Equations (3) and (4) show the mode voltages and currents of the line at distance x away from measuring point in the Laplace domain:

$$V_k\ (x, s) = F_k\ e^{-\Gamma_k\, x} + B_k\ e^{+\Gamma_k\, x} = V_{Fk}\ (x) + V_{Bk}\ (x) \tag{3}$$

$$I_k\ (x, s) = \frac{1}{Z_{ck}}\ \left(F_k e^{-\Gamma_k\, x} - B_k e^{+\Gamma_k\, x}\right) = I_{Fk}\ (x) + I_{Bk}\ (x) \tag{4}$$

$$Z_{cg} = \sqrt{\frac{Z_s + Z_m}{Y_s + Y_m}}\ ,\quad Z_{cl} = \sqrt{\frac{Z_s - Z_m}{Y_s - Y_m}} \tag{5}$$

$$F_k = \frac{V_k\,(0) + Z_k I_k\,(0)}{2}\ ,\qquad B_k = \frac{V_k\,(0) - Z_k I_k\,(0)}{2} \tag{6}$$

where $k = l, g$ denotes line and ground modes, and subscripts F and B represent the forward and backward travelling waves, respectively. Z_{ck} and Γ_k are the line characteristic impedance and the propagation coefficient of mode k. As given in Equation (6), the functions F_k and B_k are computed by voltage V_k (0) and current I_k (0) at the fault point, which are dependent on factors such as fault location and fault path resistance. According to Equations (3) and (4), when the travelling waves move along the line, the wave amplitudes are exponentially attenuated. Moreover, the polarity of forward voltage and current travelling waves and hence the polarity of their fronts is the same while the polarity of the backward waves is opposite. Considering the line end as measuring point, and the current reference direction from the line end towards the fault, the first travelling wave arriving at the measuring point is backward wave for the forward fault and it is forward wave in case of a backward fault. Therefore, it is concluded that the polarity of the first voltage and current waves arriving at the line end is opposite for a forward fault and it is the same for a backward fault.

In order to analyse the behaviour of the DC voltage and current at the line ends during an internal fault in an MTDC grid, one should consider the DC terminal illustrated in Figure 2, which connects an MMC to the DC lines. ΔV_f is the initial voltage change at the fault point and Z_f, Z_c, and Z_{conv} denote the fault impedance, the characteristic impedance, and the MMC equivalent impedance, respectively. u_{B1} and i_{B1} represent backward voltage and current waves arriving from the fault point at the end of line 1. Subscripts r and t denote reflected and transmitted parts of the backward voltage and current waves. The first incident waves arriving at the line receiving end are given by:

$$V_{Bk} = \frac{\Delta V_{fk}}{s}\ .e^{+\Gamma_k x} \tag{7}$$

$$I_{Bk} = -\frac{\Delta V_{fk}}{s Z_{ck}}.e^{+\Gamma_k x} \tag{8}$$

In a bipolar DC line, the initial change of modal voltages at the fault point of a positive pole to ground fault (PGF), and a positive pole to negative pole fault (PNF) are given as follows [32]:

$$\begin{cases} \Delta V_{fl} = \dfrac{-\sqrt{2} V_p . z_{cl}}{z_{cl} + z_{cg} + 2 z_f} \\ \Delta V_{fg} = \dfrac{-\sqrt{2} V_p . z_{cg}}{z_{cl} + z_{cg} + 2 z_f} \end{cases} \quad \text{for PGF} \tag{9}$$

$$\begin{cases} \Delta V_{fl} = \dfrac{-2\sqrt{2} V_p . z_{cl}}{2 z_{cl} + z_f} \\ \Delta V_{fg} = 0 \end{cases} \quad \text{for PNF} \tag{10}$$

The initial change of mode voltages for the negative pole to ground fault (NGF) are calculated by replacing V_p with V_n in Equation (9).

The incident wave is partly transmitted and reflected back after arriving at the line series inductor L. Using the transmission coefficient, the voltage and the current change measured at the end of the faulted line 1 are given as follows:

$$\Delta V_{1k} = \frac{2\left(sL + z_{tk}\right)}{\left(sL + z_{tk} + z_{ck}\right)} \cdot \frac{\Delta V_{fk}}{s} . e^{-\Gamma_k x} \tag{11}$$

$$\Delta I_{1k} = -\frac{2}{\left(sL + z_{tk} + z_{ck}\right)} . \frac{\Delta V_{fk}}{s} . e^{-\Gamma_k x} \tag{12}$$

$$z_{tk} = \frac{sL + z_{ck}}{m} \parallel z_{convk} \tag{13}$$

As seen, the amplitude of the incident waves decreases by increasing the fault resistance and the fault distance. It also depends on the propagation constant. As the shunt admittance in cables is higher than that in overhead lines, the attenuation and the distortion of fault-generated waves is much higher, especially in the case of long cables. The voltage and the current change measured at the end of the healthy line *i* are given as follows:

$$\Delta V_{ik} = \frac{2 z_{tk} . z_{ck}}{\left(sL + z_{tk} + z_{ck}\right) . \left(sL + z_{ck}\right)} \cdot \frac{\Delta V_{fk}}{s} . e^{-\Gamma_k x} \tag{14}$$

$$\Delta I_{ik} = \frac{2 z_{tk}}{\left(sL + z_{tk} + z_{ck}\right) . \left(sL + z_{ck}\right)} \cdot \frac{\Delta V_{fk}}{s} . e^{-\Gamma_k x} \tag{15}$$

The comparison of ΔV_{1k}, ΔV_{ik} and ΔI_{1k}, ΔI_{ik} shows that the series inductors filter out the high frequency components of the fault-generated voltage and current waves, which are transmitted from the faulted line to the terminals of the healthy lines (2 to m). It can be concluded that the fault voltage and current travelling waves measured at the faulted line end contain higher frequencies compared to those waves measured at the healthy line terminal. Therefore, it is possible to use such characteristics to discriminate the faulted line from the healthy ones. Moreover, the change of voltage and current polarity is the same for a backward fault and it is opposite in the case of a forward fault.

2.2 | Multi-resolution morphological gradient

The main idea of the mathematical morphology is to extract the information of a signal using a predefined set called structuring element (SE). The shape of SE is defined based on prior knowledge about the shape of the signal. Dilation and erosion are the two basic morphological operators, which are defined as follows [33]:

$$f \oplus g\ (x) = \max_{s} \left\{ f\,(x + s) + g\,(s) \mid (x + s) \in D_f,\ s \in D_g \right\} \tag{16}$$

$$f \ominus g\ (x) = \min_{s} \left\{ f\,(x + s) - g\,(s) \mid (x + s) \in D_f,\ s \in D_g \right\} \tag{17}$$

where D_f and D_g denote the definition domains of signals *f* and *g*, respectively. Here *g* is considered as the SE so its size must be much less than the size of the studied signal *f*. For every point within D_f, the dilation and the erosion, respectively, return the maximum and the minimum of sum and difference of *f* and *g* over the neighbourhood defined by SE.

The morphological gradient is defined as a subtraction of erosion and dilation of the signal as below:

$$MG\ (f) = \left(f \oplus g\right) - \left(f \ominus g\right) \tag{18}$$

The morphological gradient reflects the difference between the maximum and the minimum obtained by dilation and erosion within the neighbourhood defined by SE. It should be noted that the morphological gradient is affected by the size and the origin of the SE. The multi-resolution morphological gradient (MMG) is an improved morphological gradient. The main idea is to suppress the low frequency components and to enhance the high frequency transients. In order to obtain the MMG, a series of scalable flat SEs with different origins are defined as follows [33]:

$$\begin{cases} g^{+} = \left\{ g_1,\ g_2\ ,\ \ldots,\ g_{l-1}, \underline{g_l} \right\} \\ g^{-} = \left\{ \underline{g_1},\ g_2\ ,\ \ldots,\ g_{l-1}, g_l \right\} \\ \qquad l = 2^{1-a}\ l_g \end{cases} \tag{19}$$

where g^{+} and g^{-} are the SEs used for extracting the ascending and descending edges of the signal, respectively. The underlined elements in g^{+} and g^{-} denote their origins. In Equation (19), l_g is the initial length of the SEs at level 1, *a* represents the level of the MMG to be processed. By using the morphological gradient definition in Equation (18) as a reference, the dyadic MMG at level *a*, $\rho^a(g)$, is defined as:

$$\rho^a\left(g^{+}\right) = \left(\rho^{a-1} \oplus g^{+}\right)\ (x) - \left(\rho^{a-1} \ominus g^{+}\right)(x) \tag{20}$$

$$\rho^a\left(g^{-}\right) = \left(\rho^{a-1} \ominus g^{-}\right)\ (x) - \left(\rho^{a-1} \oplus g^{-}\right)(x) \tag{21}$$

$$\rho^a\ (g) = \rho^a\ \left(g^{+}\right) + \rho^a\left(g^{-}\right) \tag{22}$$

when $a = 1$, ρ^0 is the input signal. Since $(\rho^{a-1} \oplus g^{+})(x) \geq 0$ and $(\rho^{a-1} \ominus g^{+})(x) \leq 0$, then $\rho^a(\mathrm{g}^{+}) \geq 0$ and $\rho^a(\mathrm{g}^{-}) \leq 0$ correspond to the ascending and descending edges of the signal under process, respectively. Therefore, ρ_g^a can extract the information about the exact location and changing directions of the signal edges. Moreover, the increase of the level of MMG normally gives more details about the signal changes. In contrast to the theory of linear signal processing, such as Fourier and wavelet transforms, the mathematical morphology is non-linear. It is concerned with the shape of the signal waveform in the time domain instead of the frequency or time-frequency domain. As

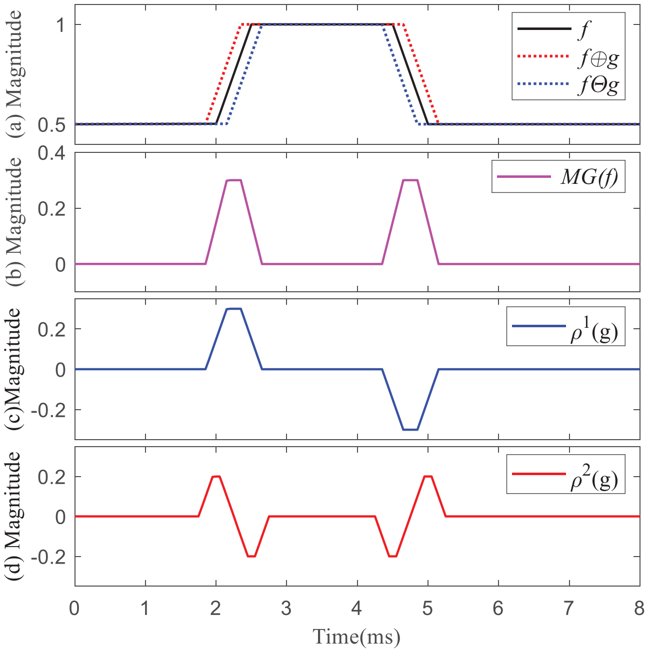

FIGURE 3 Processing of one-dimensional signal *f* with mathematical morphology

an example, the dilation, the erosion, the morphological gradient and the first and the second level MMGs of a simple one-dimensional signal, *f*, using a flat SE with the initial length of $l_g = 6$, are illustrated in Figure 3. As it can be seen, the dilation operation can be regarded as expansion, and the erosion operation as contraction. The morphological gradient detects the edges of *f* with positive values regardless of their direction. However, the MMGs detect the rising and falling edges by positive and negative peaks, respectively.

3 | PROPOSED PROTECTION METHOD

3.1 | Fault detection and pole selection

When a fault or an event occurs in the MTDC grid, the pole voltages change when the first fault-generated travelling wave arrives. The proposed protection method employs this feature to determine the faulted pole regardless of if the fault is internal or external. In order to select the faulted pole, the second level MMGs of the positive and negative pole voltages, $\rho^2(V_p)$ and $\rho^2(V_n)$,are compared to the predefined negative threshold ρ^2_{th}. At this stage, the algorithm determines the fault type. In the next stage, the fault discrimination part determines whether the fault is internal or external.

3.2 | Fault discrimination

According to Section 2, the fault-generated high frequency mode voltage and current travelling waves are attenuated after passing through the series inductors. Moreover, the voltage and current change, thus the direction of their corresponding travelling wave fronts have opposite polarities in the case of a forward fault and the same polarities for a backward fault. It is possible to use these characteristics to discriminate between internal and external faults and events. The bolted backward external faults and events such as DCCB tripping in the upstream lines can be easily discriminated from high resistance internal faults by comparing relative polarities of the voltage and current change. As the worst condition, bolted forward external faults and events such as tripping the DCCBs at downstream lines can be discriminated from high resistance internal faults. This can be done by knowing that up to a certain fault resistance, the voltage and current travelling waves of internal faults, seen at the measuring point, are more attenuated than those of the external faults and events. As mentioned, MMG can detect ascending and descending edges of a signal, so it can be used to detect the amplitude and the direction of travelling wave fronts. As seen from Equations (9) and (10), the ground mode initial voltage change at the fault point is zero in case of PNF whilst the line mode is non-zero for PGF, NGF and PNF. Therefore, the line mode is considered as an appropriate mode to define protection criterion S_l for fault discrimination as follows:

$$D_{ijL}\ (m) = \rho^2\ \left(V_{ijl}\,(m)\right).\rho^2\ \left(I_{ijl}\,(m)\right) \tag{23}$$

$$\begin{cases} S_{ijl}\,(m) \ = \displaystyle\sum_{m-2}^{m} D_{ijl}\,(m) \ < S_{thPG}, \quad PGF\ \ and\ \ NGF \\ S_{ijl}\,(m) \ = \displaystyle\sum_{m-2}^{m} D_{ijl}\,(m) \ < S_{thPN}, \quad PNF \end{cases} \tag{24}$$

here $\rho^2(V_{ijl})$ and $\rho^2(I_{ijl})$ are the second level MMGs of line mode voltage and current measured at terminal *i* of line *ij*. S_{thPG} and S_{thPN} are negative predefined thresholds for pole to ground and pole to pole faults, respectively. Since S_l represents a multiplication of the amplitude and the direction of the voltage and current change at the line terminal, when the first peak of S_l is negative then it can be concluded that the fault is internal or forward external fault, otherwise, it is backward. When S_l is smaller than the threshold, then the fault is internal, otherwise it is a forward external fault. The flowchart of the proposed protection method is illustrated in Figure 4.

4 | DEMONSTRATION OF THE PROTECTION CRITERIA

4.1 | Test system

The proposed protection method is verified by simulations performed on a four-terminal HVDC grid as shown in Figure 5. The network is modelled using the PSCAD software. The grid connects the offshore wind farms (OWFs) to the main AC grids through half-bridge MMCs and XLPE cables. Figure 6 depicts

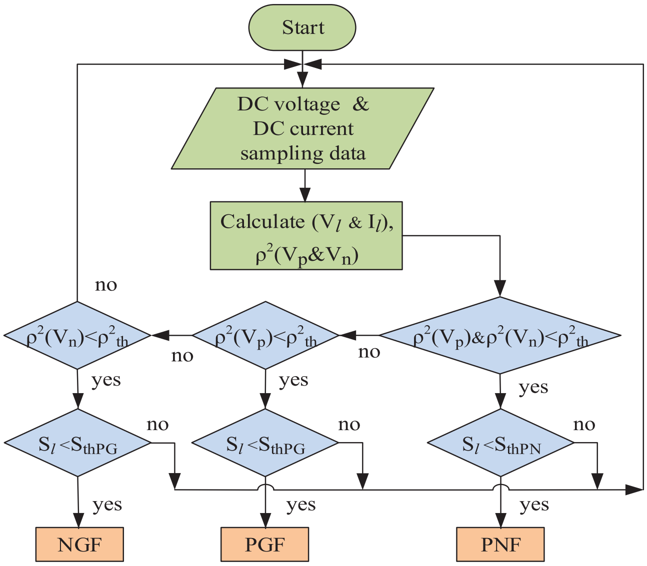

FIGURE 4 Flowchart of the proposed protection method

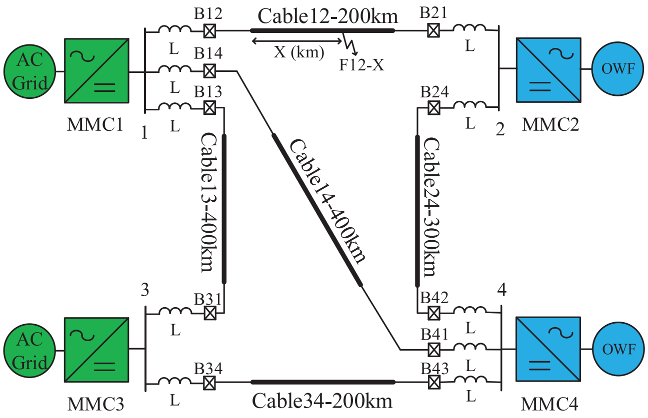

FIGURE 5 The MTDC grid test system

the cable's structure, which is represented by a frequency dependent phase model. The parameters of the AC grid, OWF and the MMCs are listed in Table 1. The configuration of the converter stations is symmetric monopole, and DC series inductors are installed at both terminals of the cable to decrease the DC current ripple and to limit the magnitude and the rate of rise of the fault current to within the interruption capability of the DCCBs [4]. The MMCs are modelled by a detailed Thevenin equivalent model of the MMC arms [34]. The DCCBs are modelled as an ideal switch in parallel to a surge arrester with a clamping voltage of 1.5 times the nominal voltage, and the earth resistivity is considered as 1 Ω m. A fault with a resistance R at an arbitrary distance X km from terminal i of line ij is denoted by F_{ij}-X-R. The voltages and currents are sampled with a sampling frequency of 20 kHz, which is a common practice in practical MTDC grids. The calculations are performed in MATLAB using a flat SE with the initial length of $l_g = 6$, and an analysis level of $a = 2$.

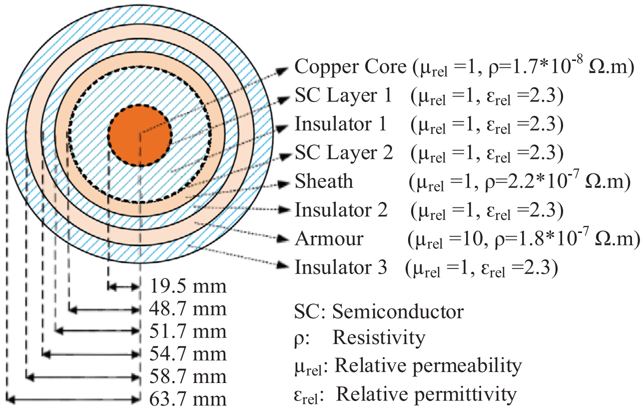

FIGURE 6 The XLPE cables structure

TABLE 1 The AC grids, windfarms and MMCs parameters

	Converter	
Parameter	**MMCs 1, 2, 4**	**MMC 3**
DC voltage	±200 kV	±200 kV
Converter AC voltage	220 kV	220 kV
Rated power	800 MW	1200 MW
Number of SMs per arm	400	400
Arm resistance R_{arm}	0.54 Ω	0.36 Ω
Arm reactor L_{arm}	29 mH	19 mH
Arm capacitance C_{arm}	25 μF	37.5 μF
Transformer leakage reactance	0.18 p.u.	0.18 p.u.
AC grids and windfarms		
AC grids voltage	380 kV	
Windfarms output voltage	145 kV	

4.2 | Assessment of the protection criteria

4.2.1 | Internal faults

Figure 7 shows the pole and mode voltages and currents, the MMG of pole and line mode voltages and currents, and the protection criterion S_l of the lines connected to terminal 1 of the test system for an internal bolted PG fault at the middle of Cable 13, PGF13-200-0. The fault inception occurs at $t = 1.5$ s. The value of the line series inductor is 50 mH, and the voltage and the current are measured at the cable terminals. As seen from Figure 7(a,e), at the initial instants after the fault inception, the rate of change of the positive pole voltage, V_{13p}, and current, I_{13p}, is higher than the corresponding quantities of the healthy cables. This results in the same scenario with regard to the line mode voltages and currents, see Figure 7(b,f). In other words, pole and mode current and voltage of the faulted line contain higher frequencies compared to the current and voltage of the healthy lines. Moreover, the rate of change of V_{13p} and V_{13l} is much higher than that of I_{13p} and I_{13l}. The second level MMG of line mode voltage, the pole voltage and the line

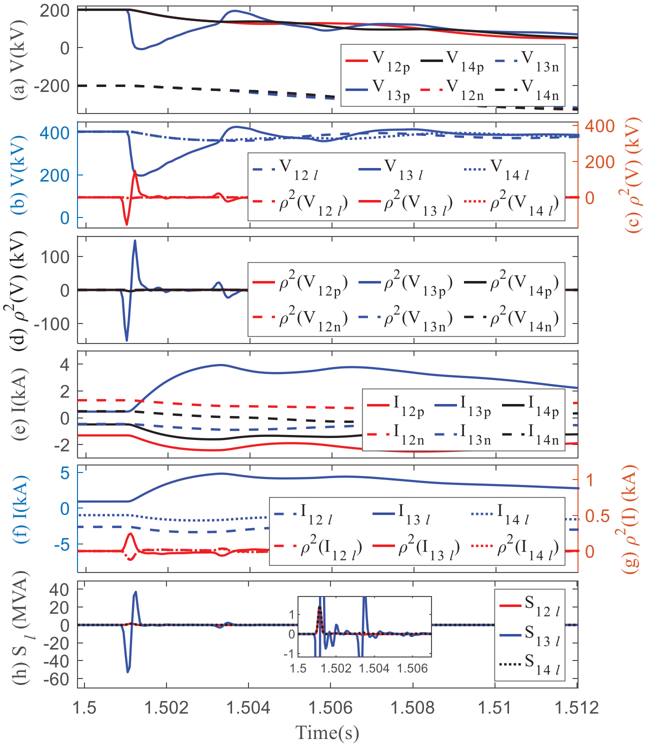

FIGURE 7 Simulation results for PGF13-200-0: (a) pole voltage, (b) line mode voltage, (C) line mode voltage MMG, (d) pole voltage MMG, (e) pole current, (f) line mode current, (g) line mode current MMG, (h) criterion S_l

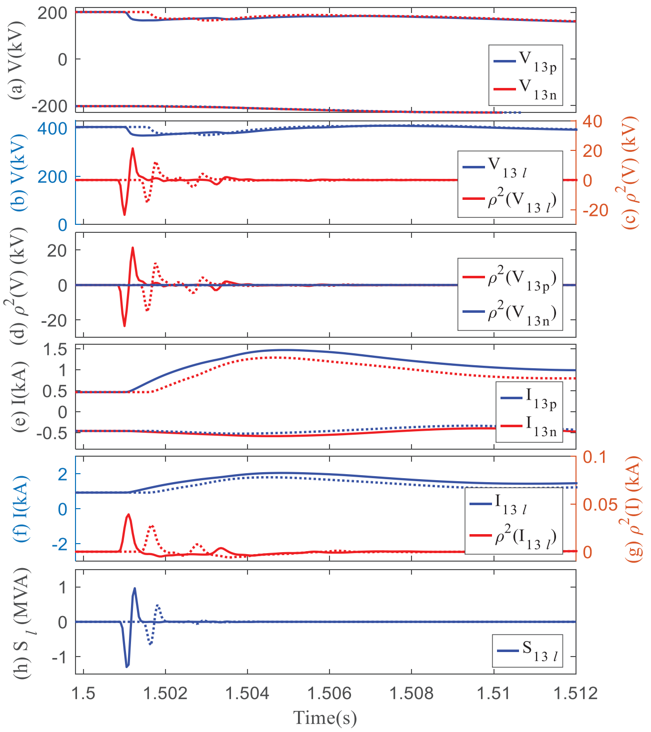

FIGURE 8 Simulation results for PGF13-200-100 (solid line) and PGF13-300-100 (dashed line)

mode current are represented in Figure 7(c,d,g), respectively. It is obvious that $\rho^2(V_{13p})$ and $\rho^2(V_{13l})$ have negative first peaks with higher amplitude compared to the other voltages. Moreover, $\rho^2(I_{13l})$ has a positive first peak, which is higher than and opposite to the first peaks of $\rho^2(I_{12l})$ and $\rho^2(I_{14l})$. The amplitude of the first peak of $\rho^2(V_{13p})$ is much higher than that of the first peak of $\rho^2(V_{13n})$ showing that the fault type is PG. The criterion S_l is shown in Figure 7(h). By the fault-generated travelling voltage and current waves arrival, S_{13l} obtains a high amplitude negative first peak that identifies the fault as a forward fault related to Cable 13. However, the values of S_{12l} and S_{14l} are positive and their first peak amplitudes are low amplitudes indicating that the fault is external. The effect of fault resistance can be addressed by comparing Figure 7 to the results for fault PGF13-200-100 in Figure 8. By increasing the fault resistance from 0 to 100 **Ω**, the peak of S_{13l} decreases from −52.8 to −1.3 MVA. This is due to the fact that the fault resistance increase reduces the initial voltage change at the fault point and corresponding travelling waves, see Equations (9) and (10). As seen in Figure 8, the change of the fault location from 200 to 300 km reduces the peak value of S_{13l} from −1.3 to −0.67 MVA. This is due to the higher attenuation of the travelling waves when passing a longer distance along the line.

4.2.2 | Close-in faults

In case of close-in faults, the travel time is very small, hence the fault-generated travelling waves are successively reflected and refracted at the line end and fault point. Depending on the sampling frequency, it may lead to inaccuracy in travelling wave front measurement and affect the protection criteria. Figures 9 and 10 demonstrate the simulation results for a close-in fault PGF13-5-0 using different sampling frequencies of 200 and 20 kHz, respectively. As shown in Figure 9, successive reflection of voltage travelling waves result in oscillation in the faulted line voltage V_{13p}. Current I_{13p} is also constituted of successive current travelling waves but it does not oscillate mainly due to the presence of the series inductor. This situation results in oscillation in $\rho^2(V_{13p})$, $\rho^2(V_{13l})$, $\rho^2(I_{13l})$ and S_{13l}. As it can be seen, the first peak of S_{13l} has a high negative value of −27 MVA indicating that the fault is internal. As shown in Figure 10, by decreasing the sampling frequency, the first peak of $\rho^2(V_{13p})$ changes from −380.2 to −386.8 MVA, the first peak of $\rho^2(V_{13l})$ changes from −380.1 to −386.3 MVA, and the first peak of $\rho^2(I_{13l})$ from 0.056 to 0.34 MVA. It should be noted that reducing the sampling frequency increases the difference between the amplitude of data samples in the wave fronts located at the neighbourhood defined by the SE. Despite losing accuracy, this issue results in detecting higher first peaks of MMG, especially in case of a current that does not oscillate. As a result, the first peak of S_{13l} changes from −27 to −199.1 MVA. Therefore, although reducing the sampling frequency from 200 to 20 kHz affects the measurement accuracy and calculated MMGs, it does not change the direction of the first peak of S_{13l} as the voltage decreases and the current increases after fault occurrence. The worst case of loss of accuracy in the waveforms occurs when the time difference between two successive peaks in the faulted line

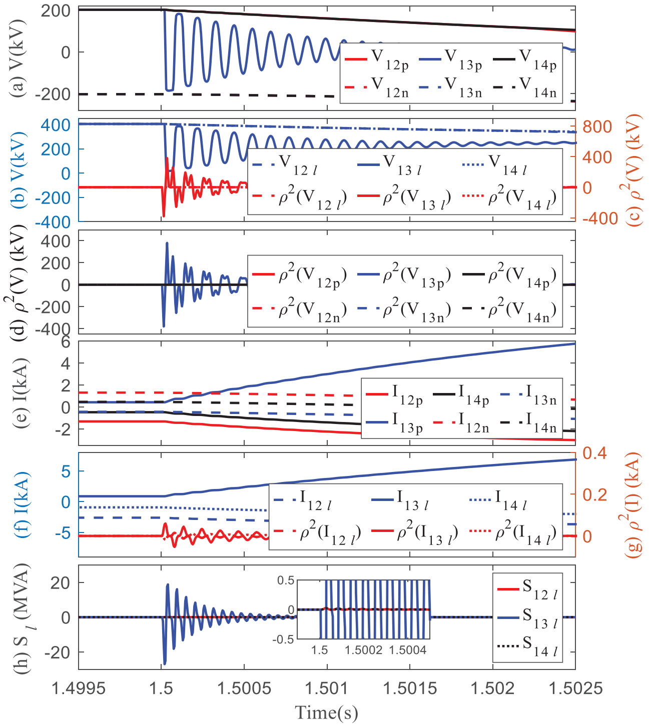

FIGURE 9 Simulation results for PGF13-5-0 with sampling frequency of 200 kHz

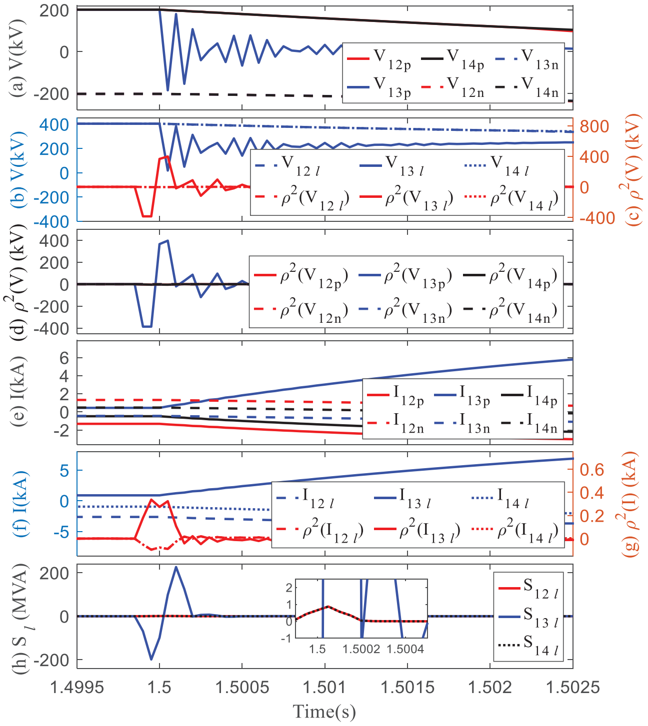

FIGURE 10 Simulation results for PGF13-5-0 with sampling frequency of 20 kHz

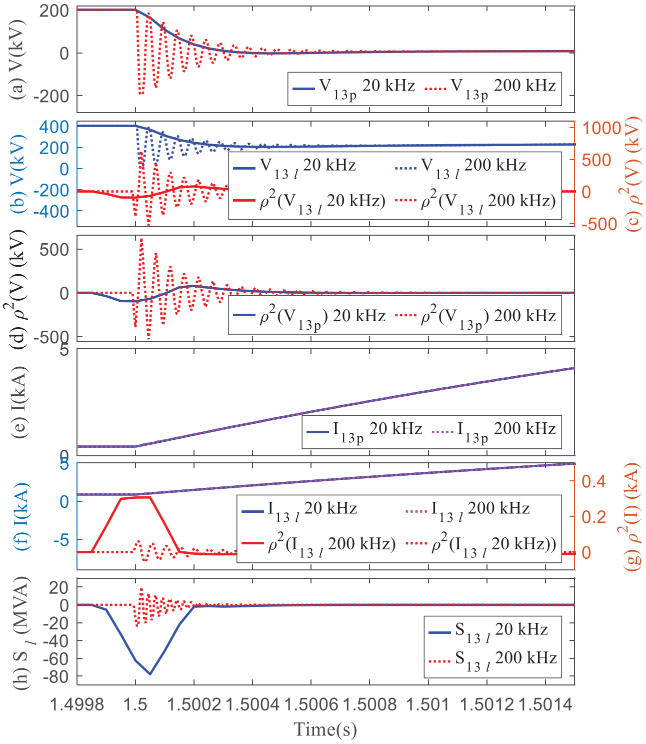

FIGURE 11 Simulation results for PGF13-2.2-0 with sampling frequency of 20 kHz

voltage waveform is equal to the sampling time interval, i.e. 50 μs for sampling frequency of 20 kHz. An example of such a situation is shown in Figure 11 by simulation of PGF13-2.2-0. By reducing the sampling frequency, the first peak of S_{13l} changes from −24 to −77.9 MVA, which correctly determines the internal fault. It can be concluded that although close-in faults result in inaccuracy of voltage and current travelling wave front, they do not affect the correct performance of the protection criteria.

4.2.3 | External faults

Figure 12 shows the simulation results for PGF12-0-0 as a backward external fault for terminal 1 of Cable 13 and Cable 14, and as a forward when the fault traveling wave reaches the cable terminal, S_{13l} and S_{14l} obtain positive peak values of 2.3 MVA, which implies that the fault is backward. However, S_{31l} does not exceed −0.03 MVA at $t = 1.5023$ s.

Table 2 shows the first peak amplitude of the protection criteria S_{13l} for different fault types, resistances and locations. Due to the symmetrical configuration of the MTDC grid, S_l is identical for the similar PG and NG faults. According to Table 2, by neglecting the bolted pole to ground close-in faults, the increase of the fault resistance and the fault distance results in a decrease of the first peak of S_l. In the case of PGF and NGF, the maximum first peak of S_{13l} for an internal fault is -0.134 MVA corresponding to PGF13-375-200 and NGF13-375-200, which is less than −0.024 MVA for the forward external faults PGF34-0-0 and NGF34-0-0. As for PNF, the maximum first peak of

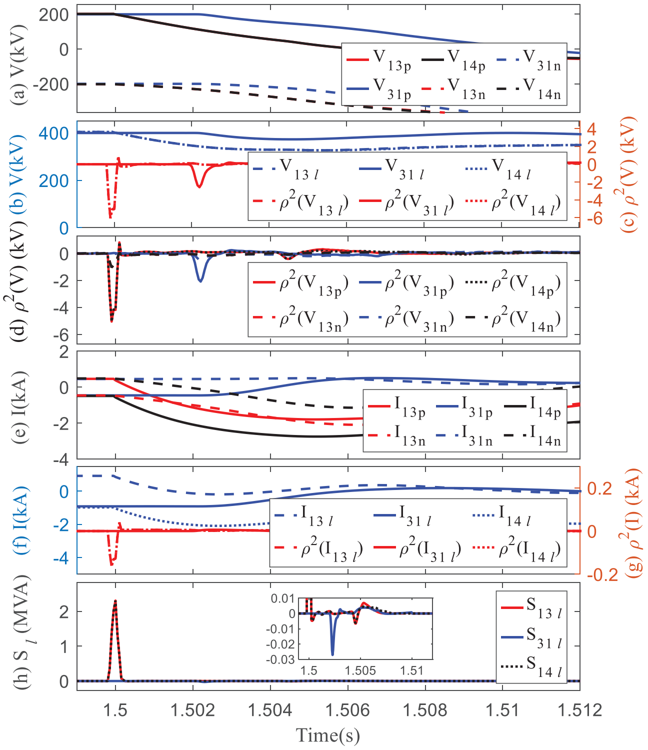

FIGURE 12 Simulation results for PGF12-0-0 as an external fault for Cable13 and Cable14

S_{13l} for an internal fault is −1.662 MVA for PNF13-375-200 while it is −0.103 MVA for the forward external fault PNF34-0-0. Therefore, it can be concluded that S_l is capable of discriminating between forward internal and external faults.

TABLE 2 First peak of S_{13l} for different faults, L_{ij} = 50 mH

Fault location	Fault type	S_{13l} $R_f = 0\ \Omega$	$R_f = 50\ \Omega$	$R_f = 100\ \Omega$	$R_f = 200\ \Omega$
F13-0	PG&NG	−123.7	−20.63	−8.223	−2.731
	PN	−502.1	−171.0	−85.21	−33.66
F13-2.2	PG&NG	−77.9	−14.95	−5.760	−1.891
	PN	−299.3	−110.7	−55.54	−22.14
F13-5	PG&NG	−199.1	−16.37	−5.592	−1.691
	PN	−411.3	−112.4	−51.24	−18.79
F13-25	PG&NG	−225.6	−16.15	−5.453	−1.645
	PN	−451.4	−116.6	−52.91	−19.46
F13-100	PG&NG	−126.8	−9.324	−3.156	−0.931
	PN	−242.6	−66.96	−30.74	−11.31
F13-200	PG&NG	−60.90	−4.388	−1.465	−0.441
	PN	−117.6	−32.10	−14.64	−5.389
F13-300	PG&NG	−30.00	−2.281	−0.776	−0.233
	PN	−56.62	−16.21	−7.541	−2.817
F13-375	PG&NG	−18.00	−1.353	−0.460	−0.134
	PN	−34.85	−9.782	−4.520	−1.662
F13-400	PG&NG	−13.73	−2.339	−0.935	−0.318
	PN	−56.46	−19.24	−9.605	−3.817
F12-0	PG&NG	0.989	0.162	0.064	0.021
	PN	0.053	1.376	0.682	0.265
F14-0	PG&NG	0.987	0.161	0.063	0.020
	PN	4.049	1.375	0.682	0.265
F34-0	PG&NG	−0.024	−0.005	−0.002	−0.000
	PN	−0.103	−0.035	−0.018	−0.008

4.3 | Tripping of DCCBs

The effect of opening DCCBs at adjacent lines is shown in Figure 13 in which B12 at the positive pole is tripped at t = 1.5s. After opening the DCCB, I_{12p} decreases to zero, the currents flow through the other lines connected to terminal 1 and associated voltages converge to steady state values. Due to the current interruption, V_{12p} decreases momentarily to a negative value and rises back to around the rated grid voltage.

Based on this, $\rho^2(V_{13p})$ reaches a high negative amplitude indicating that an event took place on the positive pole of the grid. Meanwhile, S_{12l} decreases to a first peak of −186.6 MVA while S_{13l} rises up to a maximum value of 9.95 MVA implying a backward external event. The opening of breaker B12 can be considered as a forward external event for terminal 3 of Cable13. As seen, the first peak of S_{31l} is −0.1 MVA, which is greater than the first peak of S_{311} for internal PGF13-25-200.

4.4 | Reclosing of DCCBs

At present, most of the existing VSC HVDC systems comprise cable lines. However, overhead transmission lines will be widely used due to their economic advantages over cables. Considering an overhead line (OHL) in the MTDC grid, the temporary fault is the most probable type of fault. Therefore, DCCB reclosing is needed to improve the power supply service. The effect of DCCB reclosing on the protection criteria is addressed by replacing Cable 13 with a relatively short overhead line with the length of 100 km (OHL 13) and the simulation of reclosing B13 at the positive pole at t = 1.5 s. The overhead line parameters are taken from [30]. Reclosing B13 can be considered as an internal event for terminal 3 of OHL13 that must be discriminated from internal faults. It can be also considered as a backward external event for terminal 1 of Cable 12. The simulation results are shown in Figure 14. After reclosing the DCCB, V_{13p} and V_{31p} start oscillating until obtaining new DC values, which depend on the grid and power flow conditions. The oscillation, which may take tens of milliseconds, is due to successive reflections of voltage travelling waves from the line ends. At the same time, the currents I_{13p} and I_{31p} increase from zero to their DC values. During normal operation conditions in the MTDC grid, the difference between the terminal voltages is about a few kV. Therefore, the voltage across the B13 is only a few kV before reclosing. This results in low amplitude oscillations of the voltages and

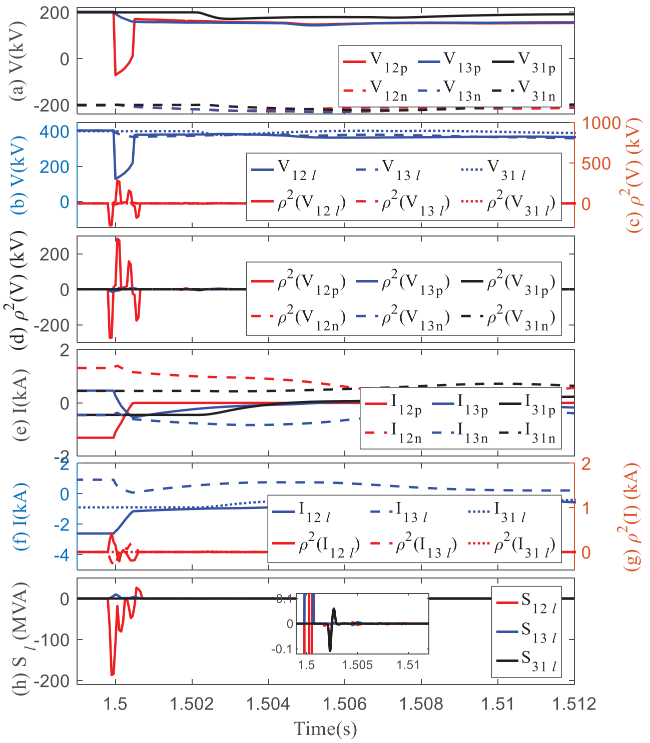

FIGURE 13 The effect of tripping DCCBs at adjacent line

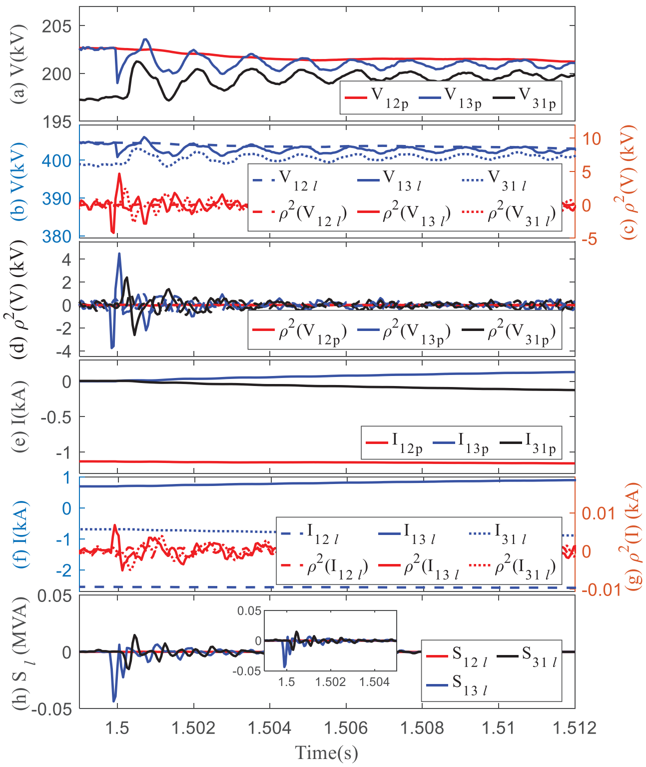

FIGURE 14 The effect of reclosing DCCB

a lower rate of rise of currents after closing the DCCB. Hence, MMGs of voltages and currents are so low that the corresponding protection criteria are small enough to distinguish between DCCB reclosing on OHL 13 and internal faults for terminal 3 of OHL 13 and for terminal 1 of Cable 12. Based on numerous simulations, it can be concluded that DCCB reclosing does not affect the performance of the proposed protection method.

4.5 | Threshold setting

As shown by the simulation results, the first peak of the protection criterion S_l takes a negative high value for internal faults and a negative low value for forward external faults and events such as DCCB opening. It also has a positive value in the case of backward external faults and events. Therefore, in order to determine the thresholds S_{thPG} and S_{thPN}, it is sufficient to consider a margin between the maximum value of the first peak of S_l for high resistance internal faults and the minimum value of the first peak of the same criteria in the case of bolted forward external faults and DCCB opening at the adjacent line. The threshold S_{thPG} is set according to the calculation of the aforementioned maximum and minimum values of the first peak of S_l by the simulation of pole to ground faults and DCCB opening at one pole. S_{thPN} is determined considering PN faults and DCCB opening at both positive and negative poles. By analysis of pole to ground and pole to pole faults, Figure 15 shows maximum first peak of S_l for internal faults, and minimum first peak of S_l for external faults, as well as DCCB opening as a forward external event. The thresholds are calculated considering internal faults with a resistance of 200 Ω and bolted external faults, as well as series inductor sizes of 50 and 100 mH. As illustrated, the increase in inductor size results in a decrease in S_l for both internal and external faults and DCCB opening as well. However, the decrement of S_l for external faults and DCCB opening is higher. This allows to have higher margin between S_{th} and S_l and to increase the dependability and security of the method. ρ^2_{th} is determined by obtaining the maximum first peak of $\rho^2(V_p$ and $V_n)$ in case of high resistance internal pole to ground faults. By applying large number of simulations, the value of ρ^2_{th} is set to −5 kV.

5 | EVALUATION OF THE METHOD

The robustness of the proposed protection method is analysed for the test MTDC grid depicted in Figure 5, for different cases of internal and external DC faults, and external AC faults. The method is also verified for an overhead transmission line.

5.1 | Internal faults

In order to assess the effectiveness of the protection method under internal fault conditions, PG and PN faults on the cables in the MTDC grid are simulated at $t = 1.5$ s. In order to consider both far-end and near-end faults, fault locations at 10 km away from the sending end of each cable are observed. Due to the symmetrical configuration of the MTDC grid, PG and NG

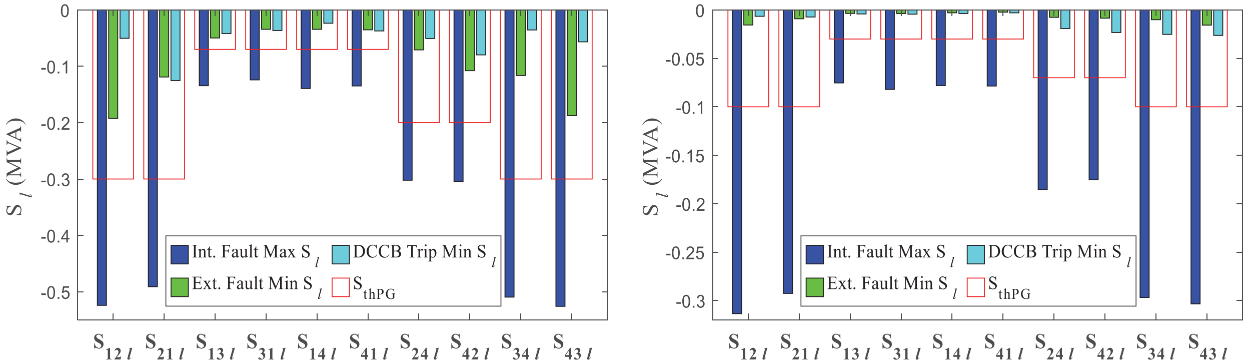

(a) PG&NG faults, R_f=200 ohm, L_{ij}=50mH

(c) PG&NG faults, R_f=200 ohm, L_{ij}=100mH

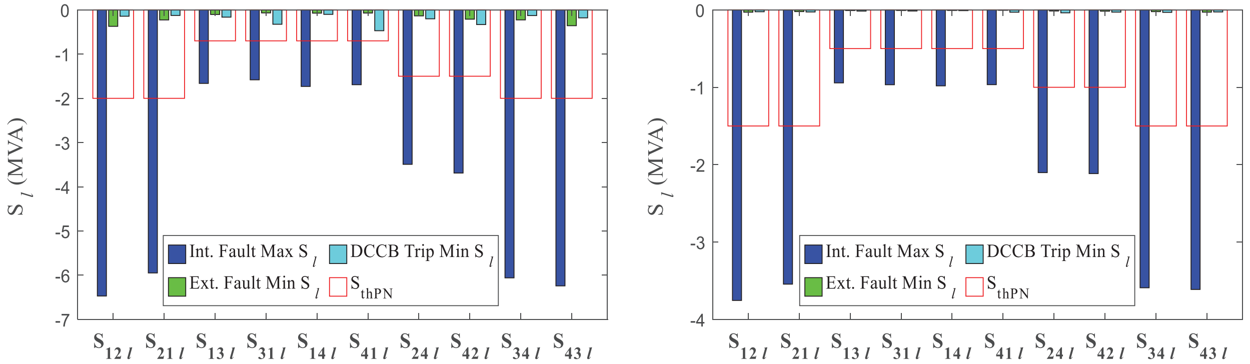

(b) PN faults, R_f=200 ohm, L_{ij}=50mH

(d) PN faults, R_f=200 ohm, L_{ij}=100mH

FIGURE 15 Threshold settings for the proposed protection method applied to the MTDC grid test system

TABLE 3 Performance of the protection method in case of internal faults, L_{ij} = 50 mH, R_f = 50 Ω

Fault point	Fault type	S		$\rho^2(V_p)$	Operation time (ms)	Fault detection
F12-10	PG	S_{12l}	−11.48	−98.83	0.3	Cable 12
		S_{21l}	−2.98	−45.13	1.35	
	PN	S_{12l}	−82.57	−131.72	0.3	Cable 12
		S_{21l}	−20.01	−59.74	1.35	
F13-10	PG	S_{13l}	−11.42	−98.63	0.3	Cable 13
		S_{31l}	−0.81	−21.22	2.5	
	PN	S_{13l}	−82.26	−131.50	0.3	Cable 13
		S_{31l}	−5.25	−27.02	2.5	
F14-10	PG	S_{14l}	−11.43	−98.74	0.3	Cable 14
		S_{41l}	−0.86	−21.06	2.45	
	PN	S_{14l}	−82.28	−131.56	0.3	Cable 14
		S_{41l}	−5.59	−26.92	1.9	
F24-10	PG	S_{24l}	−11.02	−100.97	0.3	Cable 24
		S_{42l}	−1.74	−30.69	1.9	
	PN	S_{24l}	−79.59	−134.17	0.3	Cable 24
		S_{42l}	−12.10	−40.90	1.9	
F34-10	PG	S_{34l}	−10.55	−98.48	0.3	Cable 34
		S_{43l}	−3.12	−44.43	1.35	
	PN	S_{34l}	−75.87	−130.84	0.3	Cable 34
		S_{43l}	−20.88	−59.00	1.35	

TABLE 4 Performance of the protection method in case of external faults, $L_{ij} = 50$ mH, $R_{\mathrm{f}} = 0\ \Omega$

Fault	S_{13l} and S_{31l}		Fault detection
PGF12-10	S_{13l}	0.6360	External fault
	S_{31l}	−0.0058	
PGF14-10	S_{13l}	0.6347	External fault
	S_{31l}	−0.0058	
PGF24-10	S_{13l}	0.0005	External fault
	S_{31l}	0.0005	
PGF34-10	S_{13l}	−0.0091	External fault
	S_{31l}	0.9280	

TABLE 5 Performance of the protection method in case of external AC faults, $L_{ij} = 50$ mH, $R_{\mathrm{f}} = 0\ \Omega$

Min of $\rho^2(V)$	F1-ac grid	F2-OWF	F3-ac grid	F4- OWF
$\rho^2(V_{12p})$	−0.0448	−0.1746	−0.0443	−0.0470
$\rho^2(V_{21p})$	−0.0708	−0.4307	−0.0778	−0.0305
$\rho^2(V_{13p})$	−0.0333	−0.0343	−0.0367	−0.0342
$\rho^2(V_{31p})$	−0.0624	−0.0529	−0.0149	−0.0529
$\rho^2(V_{14p})$	−0.0166	−0.0308	−0.0398	−0.0308
$\rho^2(V_{41p})$	−0.0310	−0.0310	−0.0310	−0.0720
$\rho^2(V_{24p})$	−0.0805	−0.4517	−0.0248	−0.1088
$\rho^2(V_{42p})$	−0.0287	−0.1283	−0.0147	−0.0737
$\rho^2(V_{34p})$	−0.0757	−0.0757	−0.0568	−0.0899
$\rho^2(V_{43p})$	−0.0369	−0.0293	−0.0293	−0.0941

TABLE 6 Performance of the method for OHL 13

Fault	S_{13l}	$\rho^2(V_p)$	Operation time (ms)	Fault detection
PGF13-0-300	−24.4	−91.9	0.4	Internal
PGF13-25-300	−20.8	−112	0.5	Internal
PGF13-100-300	−13.3	−76.7	0.8	Internal
PGF13-200-300	−7.47	−54.8	1.1	Internal
PGF13-300-300	−4.52	−38.8	1.4	Internal
PGF13-400-300	−3.32	−33.7	1.6	Internal
PGF13-500-300	−2.28	−27.7	2	Internal
PGF13-600-300	−1.98	−25.6	2.3	Internal
PGF13-700-300	−1.67	−22	2.7	Internal
PGF13-800-300	−1.40	−20.4	3	Internal
PGF13-875-300	−1.53	−20.1	3.3	Internal
PGF13-900-300	−1.45	−19.1	3.4	Internal
PGF12-0-0	6.85	−37.6	NA	External
PGF14-0-0	6.85	−37.6	NA	External
PGF34-0-0	−0.48	−10.2	NA	External

faults behave identically, so NG faults are not presented in this paper. The simulation results presented in Table 3 show that in all the cases, the faulted cable is identified correctly, and the protection criteria have acceptable discrimination with their thresholds. The maximum fault detection operation time is 2.5 ms for Cable 13 with 400 km length, in which the fault distance from the measuring terminal is 390 km. In fact, the operation time includes the arrival time of the travelling wave at the measuring terminal, the time of data sampling and transferring at the bus level and a very short time for the calculation of the protection criteria by the use of multi-resolution morphological gradient. The required time for the proposed method to detect and discriminate the fault is equal to the time needed to take a few voltage and current samples after the travelling waves arrive at the measurement point, i.e. 6 samples for the computation of $\rho^2(V)$ and 6 samples for the calculation of S_l, which result in $12 \times 50\ \mu\mathrm{s} = 0.6$ ms, considering the sampling frequency of 20 kHz.

5.2 | External faults

The results of the stability of the protection method against external DC faults are shown in Table 4, in which bolted PG faults on Cables 12, 14, 24, and 34 are simulated as external faults for Cable 13. The results confirm that in all the cases, the faults are successfully identified by S_{13l} and S_{31l} as external faults for Cable 13.

The proposed method is also robust in discriminating external faults on the OWFs and AC grids from internal faults. In order to evaluate the security of the method against external AC faults, three-phase bolted faults are simulated at the connection points of the OWFs and the AC grids to the MTDC grid. The simulation results provided in Table 5 show that the external AC faults have almost no impact on $\rho^2(V)$, so the algorithm does not react to these faults.

5.2.1 | Performance of the method for overhead lines

To evaluate the performance of the protection method in case of overhead lines, the length of OHL 13 used in Section 4.4 is changed to 900 km. The performance of the method is illustrated in Table 6 for high resistance internal PG faults as well as bolted backward and forward external PG faults incepted at $t = 1.5$ s. The fault resistance is 300 Ω and series inductor size is 50 mH. According to Table 6, the method is capable of protecting the OHL against the internal faults and it is secure against the external ones.

6 | COMPARISON WITH OTHER METHODS

The proposed method is compared to other non-unit protection methods as shown in Table 7. The methods are compared for selected line type and length, fault resistance, series inductor size, sampling rate, fault detection time and required signals. The fault detection time is defined as the time required by the method to detect and discriminate the fault after the first

TABLE 7 Comparison of the proposed method with other works

Ref. no.	Line type	Line length (km)	R_f (Ω)	L_{ij} (mH)	Sampling rate (kHz)	Detetion time (ms)	Signals used
Pro. method	CableOHL	400900	200300	50	20	<0.6	V&I
[3]	Cable	400	0.01	50	20	<0.7	V
[9]	CableOHL	5001500	NA	50	NA	NA	V
[10]	CableOHL	500 1500	50100	40	25	<0.2	V
[11]	OHL	450	20	50	100	<12	V&I
[12]*	CableOHL	150	1000	200	200	<0.5	V
[13]	OHL	200	300	150	NA	<1	V
[14]	CableOHL	100 200	200	10	10	<1.5	V
[15]	OHL	208	400	200	100	<1	V&I
[23]	Cable	200	10	NA	2	<1.5	I
[26]	OHL	184	300	200	1000	<1.2	V
[27]	CableOHL	200400	300	100	10	<2	V&I
[28]	OHL	500	300	100	200	<1	I
[29]	OHL	908	300	150	10	<3	V&I
[30]	CableOHL	200800	200	100	20	<0.3	V
[31]	Cable	200	NA	20	10	<1.7	V&I

*Tested only for PN faults.

travelling wave arrives at the cable terminal. It can be seen the proposed method is faster than all the methods except the methods proposed in [10, 12, 30]. By taking into account the line length and the maximum fault resistance, the proposed method gives superior performance compared to all the other methods for the protection of cables. Regarding OHL, the proposed method is comparable to the method in [29] as the most capable method in the protection of OHLs, and it can be seen that the proposed method is much faster. The method requires voltage and current measurement with a reasonable sampling rate of 20 kHz, which is a common practice for HVDC applications. Therefore, requiring both voltage and current signals does not limit its application.

7 | CONCLUSION

A non-unit directional protection method based on MMG of the line mode DC voltage and current with predefined thresholds is proposed to protect very long transmission lines in MTDC grids. The method is based on the magnitude and the relative direction of voltage and current travelling wave fronts determined by the multiplication of MMG of voltages and currents measured at the line terminals. The method also deploys the MMG of the voltage to determine the faulted pole. The threshold settings are determined by performing numerous simulations on the under study MTDC grid and then comparing the obtained protection criteria for internal faults, external faults, and DCCB opening on the other lines. As the method uses local measurements, it does not require a communication link between the line ends. Moreover, it only needs a relatively low sampling rate of 20 kHz, which is common in practical MTDC systems. The method performance is verified for internal and external DC faults, as well as external AC faults. The results and the analysis show that the applied methodology is robust in detecting faults accurately in less than 0.6 ms. This has been verified through numerous cases performed for different cable and OHL lengths, fault resistance, and series inductors. The simulation tests confirm the dependability, security and speed of the method for protection of very long HVDC cables and OHL.

ORCID

Marjan Popov https://orcid.org/0000-0001-7292-5334

REFERENCES

1. Koutiva, X.I., et al.: Optimal integration of an offshore wind farm to a weak grid. IEEE Trans. Power Delivery 21, 987–994 (2006)
2. Xu, L., Yao, L., Sasse, C: Grid integration of large DFIG-based wind farms using VSC transmission. IEEE Trans. Power Syst. 22, 976–984 (2007)
3. De Kerf, K., et al: Wavelet-based protection strategy for DC faults in multi-terminal VSC HVDC systems. IET Gener. Transm. Distrib. 5, 496–503 (2011)
4. Cwikowski, O., et al.: Fault current testing envelopes for VSC HVDC circuit breakers. IET Gener. Transm. Distrib. 10, 1393–400 (2016)
5. Liu, S., et al.: Modelling, experimental validation and application of VARC HVDC circuit breakers. IEEE Trans. Power Delivery 35, 1515–1526 (2019)
6. Bucher, M.K., Franck, C.M: Contribution of fault current sources in multiterminal HVDC cable networks. IEEE Trans. Power Delivery 28, 1796–1803 (2013)
7. Tang, L., Ooi, B.T: Locating and isolating DC faults in multi-terminal DC systems. IEEE Trans. Power Delivery 22, 1877–1884 (2007)
8. Yang, J., Fletcher, J.E., O'Reilly, J: Multiterminal DC wind farm collection grid internal fault analysis and protection design. IEEE Trans. Power Delivery 25, 2308–2318 (2010)
9. Sneath, J., Rajapakse, A.D: Fault detection and interruption in an earthed HVDC grid using ROCOV and hybrid DC breakers. IEEE Trans. Power Delivery 31, 973–981 (2016)

10. Haleem, N.M., Rajapakse, A.D: Local measurement based ultra-fast directional ROCOV scheme for protecting Bi-pole HVDC grids with a metallic return conductor. Int. J Electr. Power Energy Syst. 98, 323–330 (2018)
11. Stumpe, M., et al.: DC fault protection for modular multi-level converter-based HVDC multi-terminal systems with solid state circuit breakers. IET Gener. Transm. Distrib. 12, 3013–20 (2018)
12. Li, R., Xu, L., Yao, L: DC fault detection and location in meshed multi-terminal HVDC systems based on DC reactor voltage change rate. IEEE Trans. Power Delivery 32, 1516–1526 (2017)
13. Li, C., Gole, A.M., Zhao, C: A fast DC fault detection method using DC reactor voltages in HVDC grids. IEEE Trans. Power Delivery 33, 2254–2264 (2018)
14. Liu, J., Tai, N., Fan, C: Transient-voltage-based protection scheme for DC line faults in the multiterminal VSC-HVDC System. IEEE Trans. Power Delivery 32, 1483–1494 (2017)
15. Huang, Q., et al.: A non-unit line protection scheme for MMC-based multi-terminal HVDC grid. Int. J. Electr. Power Energy Syst. 107, 1–9 (2019)
16. Descloux, J., Raison, B., Curis, J.B: Protection strategy for undersea MTDC grids. In: IEEE Grenoble Conference. Grenoble, 1–6 (2013)
17. Gao, S., Liu, Q., Song, G: Current differential protection principle of HVDC transmission system. IET Gener. Transm. Distrib. 11, 1286–1292 (2016)
18. Gao, S., et al.: Novel pilot protection principle for high-voltage direct current transmission lines based on fault component current characteristics. IET Gener. Transm. Distrib. 9, 468–474 (2015)
19. Song, G., et al.: A novel pilot protection principle for VSC-HVDC cable lines based on fault component current. Int. J. Electr. Power Energy Syst. 53, 426–433 (2013)
20. Zhao, P., Chen, Q., Sun, K: A novel protection method for VSC-MTDC cable based on the transient DC current using the S transform. Int. J. Electr. Power Energy Syst. 97, 299–308 (2018)
21. Azizi, S., et al.: A traveling-wave-based methodology for wide-area fault location in multiterminal DC systems. IEEE Trans. Power Delivery 29, 2552–2560 (2014)
22. Azizi, S., Afsharnia, S., Sanaye-Pasand, M: Fault location on multi-terminal DC systems using synchronized current measurements. Int. J. Electr. Power Energy Syst. 63, 779–86 (2014)
23. Bertho, R., et al.: Selective nonunit protection technique for multiterminal VSC-HVDC grids. IEEE Trans. Power Delivery 33, 2106–2114 (2017)
24. Tzelepis, D., et al.: Single-ended differential protection in MTDC networks using optical sensors. IEEE Trans. Power Delivery 32, 1605–1615 (2016)
25. Leterme, W., Van Hertem, D: Cable protection in HVDC grids employing distributed sensors and proactive HVDC breakers. IEEE Trans. Power Delivery 33, 1981–1990 (2018)
26. Tang, L., et al.: A high-speed protection scheme for the DC transmission line of a MMC-HVDC grid. Electr. Power Syst. Res. 168, 81–91 (2019)
27. Li, B., et al.: A novel single-ended transient-voltage-based protection strategy for flexible DC grid. IEEE Trans. Power Delivery 34, 1925–1937 (2019)
28. Zhang, C., et al.: An improved non-unit traveling wave protection method with adaptive threshold value and its application in HVDC grids. IEEE Trans. Power Delivery 35, 1800–1811 (2020)
29. Li, B., et al.: An improved transient traveling-wave based direction criterion for multi-terminal hvdc grid. IEEE Trans. Power Delivery 35, 2517–2529 (2020)
30. Jamali, S., Mirhosseini, S.S: Protection of transmission lines in multi-terminal HVDC grids using travelling waves morphological gradient. Int. J. Electr. Power Energy Syst. 108, 125–34 (2019)
31. Liu, L., et al.: A fast protection of multi-terminal HVDC system based on transient signal detection. IEEE Trans. Power Delivery 36, 43–51 (2021)
32. Zhang, Y., Tai, N., Xu, B: Fault analysis and traveling-wave protection scheme for bipolar HVDC lines. IEEE Trans. Power Delivery 27, 1583–1591 (2012)
33. Wu, Q.H., Lu, Z., Ji, T.Y: Protective relaying of power systems using mathematical morphology. Springer Science & Business Media, New York (2009)
34. Gnanarathna, U.N., Gole, A.M., Jayasinghe, R.P: Efficient modeling of modular multilevel HVDC converters (MMC) on electromagnetic transient simulation programs. IEEE Trans. Power Delivery 26, 316–324 (2011)

How to cite this article: Mirhosseini SS, Jamali S, Popov M. Non-unit protection method for long transmission lines in MTDC grids. *IET Gener Transm Distrib*. 2021;1-14. https://doi.org/10.1049/gtd2.12125